

RESEARCH ARTICLE

WILEY

Shape optimization for the strong directional scattering of dielectric nanorods

Juan C. Araújo¹  | Eddie Wadbro^{1,2} 

¹Department of Computing Science,
Umeå University, Umeå, Sweden

²Department of Mathematics and
Computer Science, Karlstad University,
Karlstad, Sweden

Correspondence

Juan C. Araújo, Department of
Computing Science, Umeå University,
SE-901 87 Umeå, Sweden.
Email: jaraujo@cs.umu.se

Abstract

In this project, we consider the shape optimization of a dielectric scatterer aiming at efficient directional routing of light. In the studied setting, light interacts with a penetrable scatterer with dimension comparable to the wavelength of an incoming planar wave. The design objective is to maximize the scattering efficiency inside a target angle window. For this, a Helmholtz problem with a piecewise constant refractive index medium models the wave propagation, and an accurate Dirichlet-to-Neumann map models an exterior domain. The strategy consists of using a high-order finite element (FE) discretization combined with gradient-based numerical optimization. The latter consists of a quasi-Newton (BFGS) with backtracking line search. A discrete adjoint method is used to compute the sensitivities with respect to the design variables. Particularly, for the FE representation of the curved shape, we use a bilinear transfinite interpolation formula, which admits explicit differentiation with respect to the design variables. We exploit this fact and show in detail how sensitivities are obtained in the discrete setting. We test our strategy for a variety of target angles, different wave frequencies, and refractive indexes. In all cases, we efficiently reach designs featuring high scattering efficiencies that satisfy the required criteria.

KEYWORDS

directional scattering, Helmholtz problem, light routing, scattering problem, shape optimization

1 | INTRODUCTION

In the transition from electronics to photonics technology, the ability to control the propagation, confinement, and emission of light has become of paramount importance in the development of faster and more reliable technologies. Specifically, the so-called light routing has application in photovoltaics, on-chip light routing for integrated optical circuits, field-enhanced and surface-enhanced spectroscopy, ultracompact nanoantennas, as well as metalenses to name a few. Of particular interest is the directional routing of light or directional scattering by dielectric scatterers, which is the main topic of this work.

The problem setup consists of a penetrable scatterer that is illuminated by an incoming planar wave. We are particularly interested in cases where the source wavelength is of the order of the size of the scatterer, and thus near field computations are required. The time harmonic Maxwell equations models the physical phenomena and, for nonmagnetic

This is an open access article under the terms of the Creative Commons Attribution-NonCommercial-NoDerivs License, which permits use and distribution in any medium, provided the original work is properly cited, the use is non-commercial and no modifications or adaptations are made.

© 2021 The Authors. *International Journal for Numerical Methods in Engineering* published by John Wiley & Sons Ltd.

materials, the scattering strength is described by the dielectric constant. The problem is reduced to a scalar Helmholtz equation by considering cylindrical scatterers of infinite length and requiring a transverse polarization of the incoming wave.

The objective of the optimization is to find the shape of the scatterer that maximizes the scattering efficiency at a target angle window when illuminated by a plane wave of fixed frequency. Here the scattering efficiency is the quotient between the time-averaged Poynting vector over a target angle window and its complement. The problem falls under the class of PDE-constrained shape optimization problems, where the sensitivity of the shape of the scatterer is driven by the scattered wave, which is constrained to satisfy Helmholtz equation subject to an outgoing wave condition.

The PDE is discretized by a high-order polynomial version of the finite element method and the outgoing wave condition is modeled by an accurate Dirichlet-to-Neumann (DtN) map. We use a fixed number of elements, which has the advantage of avoiding difficulties related with remeshing. The objective function is evaluated after a solution to the PDE is computed, and the sensitivities of the design variables are obtained by using a discrete adjoint method. The numerical optimization consists of the BFGS method with backtracking line search.

1.1 | Overview

The optimization of the scattering properties of a given shape prototype has traditionally been pursued by employing intuition-based approaches. The aim is to enhance specific features of the scattering response of a candidate shape by tuning a small set of its characteristic parameters, which can be tested by using representation formulas. The end result are devices that exhibit extraordinary optical properties.

The shape prototype is often selected from a gallery of candidates by having some a priori knowledge on its scattering response. Thereafter, a small set of design variables is defined to contain few of the geometrical parameters (radius of a cylinder,^{1,3} eccentricity of an spheroid/ellipsoid,^{4,8} or thickness of a coating layer^{4,6}) and material parameters (metal^{3,4,6,9,10} or all-dielectric^{1,2,5,6,8}). Finally, for a given frequency, the design variables are fine-tuned in order to satisfy an optimal criteria. Common goals are the maximization or minimization of the so-called back-scattering and forward-scattering.^{1,5-9,11,12}

On scatterers with simple convex shapes the scattering of incident waves can be expressed by the use of representation formulas, where the scattering amplitude is given as a function of the evaluation point and the frequency of the incoming wave. The optical constants and the geometrical parametrization of the scatterer enter the formulas as parameters of the model. The so-called Mie series^{1,5,6,13} or multipole expansions^{3,9,12,14} are commonly used for the optimization of the directional scattering of light. After truncation of the series, the representation formulas result in a relatively simple system of algebraic equations at the evaluation point. The scattering efficiency can be optimized by direct manipulation of the resulting equations, which allows for the fine-tuning of the design variables.

An alternative approach is to combine the individual scattering response of few highly symmetric shapes such that the resulting interference from each of the representation formulas^{1,4,5,8-10,14} yield the desired scattering properties.

Although traditional approaches are successfully in use today, they suffer from important limiting factors. An optimization framework relying on representation formulas may be too restrictive. An early truncation of the series representation may lead to missing important features of the problem, and working with many terms may render the optimization strategy impractical. Additionally, there is no clear path on how to propose new candidates into the gallery of templates, or how to achieve better functionality of a known prototype.

Instead of the techniques described above, an optimal design strategy can be employed. Then, the problem is modeled as a PDE, and a set of design variables is used to represent the refractive index profile. Finally, the search for the optimal shape requires the computation of the sensitivities of a target objective function with respect to the design variables. Alternative formulations for gradient-based numerical optimization are the so-called density-based topology optimization (Jensen and Sigmund¹⁵) and the Level-set topology optimization (Burger et al.¹⁶). For these schemes, the number of design variables is typically proportional to the number of elements in the FE mesh and the dimension of the employed FE space, respectively.

In density-based topology optimization, the permittivity function is typically represented as a piecewise constant function. That is, at each element of the FE mesh, a constant permittivity value is assigned. The optimal design consists of a permittivity profile that optimizes the objective function. To avoid nonphysical regions with intermediate permittivities and obtain desired results, the solution scheme for the density-based approach typically includes a penalization step and a filtering process. To achieve high design freedom using a piecewise constant permittivity, density-based topology

optimization typically employs a large number of elements and design variables. A large number of elements motivates the use of a low-order FE, which has some drawbacks discussed below.

In the level set method, a given design is described by splitting the physical domain Ω into level sets of a function that varies continuously over space. Then, by introducing a binary splitting, a partitioning is defined depending on the sign of the level set function. The interface between the different media is represented as the set of points where the level set function is zero. To search for an optimal design, the level set function is evolved either through an equation of motion or via gradients until a local minimum is reached. For a recent review on design optimization in nanophotonics see Molesky et al.¹⁷

In the current work, the proposed strategy focuses on the displacement of the nodal values at the shape interface. A finite Fourier parametrization is used for the geometrical representation of shapes, which can be easily enlarged to allow for complex shapes. The set of design variables are the coefficients of the finite Fourier representation. At the discrete level, we employ a transfinite interpolation, which allows the opportunity for using a high-order FE discretization of the PDE. Finally, an exact discrete adjoint method is used for obtaining the sensitivity of a target objective function with respect to the design variables.

The advantage of high-order FEM for wave scattering problems with smooth interfaces is greatly experienced when comparing dispersive pollution error of low-order versus high-order FE. Pre asymptotic error estimation predicts that increasing the polynomial degree p is more efficient than decreasing the mesh size h . The works by Araújo et al.^{18,19} present results for scattering resonance computations by comparing the resulting errors obtained by refining p and h , respectively. Particularly, h refinements consists on fixing p and decreasing h uniformly over the mesh, and p refinements consists of increasing p uniformly and keeping h fixed. For resonators with smooth interfaces the results from computations indicate that using a uniform high polynomial degree combined with coarse cells is overall a better strategy than using a low polynomial degree combined with a fine mesh. This, from the accuracy of the solutions and performance of the solver.^{18,19} These conclusions can also be drawn for the scattering problems treated in this work. We emphasize this point in Section 3.5.1 where formula (62) gives a pre asymptotic estimate for controlling the pollution error.

A clear advantage of the Fourier parametrization is that we can obtain very complex shapes by using a relatively small number of design variables. Thus the linear system solve at each iteration of the BFGS is relatively inexpensive, which can be compared with the cost of using BFGS with, for example, the gradients arising in the density-based or the level set topology optimization formulations. The latter methods use many design variables and typically require additional steps, such as filtering or reinitializations.

In the following sections, we describe in detail the employed methodology and finalize by showing the numerical results for a range of experiments over frequency, refractive indexes, and target angles.

2 | OPTIMIZATION PROBLEM AND PARAMETRIZATION

2.1 | Governing equations

In the following, we consider nonmagnetic, locally homogeneous, and isotropic materials, and assume the time harmonic ansatz $e^{-i\omega t}$, with $\omega \in \mathbb{R}$ a given frequency. From the Maxwell equations, we obtain a decoupled wave equation^{20,21} for the electric field \mathbf{E}

$$\nabla \times \nabla \times \mathbf{E} - \left(\frac{\omega}{c}\right)^2 \varepsilon \mathbf{E} = 0, \quad (1)$$

where c is the speed of light in vacuum, and the complex relative permittivity ε accounts for the description of dielectrics and metals in the optical regime.²²

2.1.1 | Infinite length along the x_3 -axis

Dielectric cylinders with infinite length along the x_3 -axis are represented by using $\varepsilon = \varepsilon(x_1, x_2, \omega)$, which is independent of x_3 . This particular symmetry suggests the following explicit separation of variables

$$\mathbf{E} := \tilde{\mathbf{E}}(x_1, x_2) e^{ik_3 x_3}. \quad (2)$$

Moreover, we assume that the incoming plane wave has the following polarization:

Transverse magnetic (TM) polarized waves: In this case the electric field has the explicit form $\tilde{\mathbf{E}} := (0, 0, u)^\top$. From (1) and (2), we obtain the equivalent problem

$$-\Delta u - \omega^2 n^2 u = 0, \quad \text{for } x \in \mathbb{R}^2, \quad (3)$$

where $n^2 := \varepsilon(x, \omega)/c^2$ is the square of the *refractive index*. From the suggested cylindrical symmetry, the three-dimensional vector problem (1) is reduced to the equivalent two-dimensional scalar problem (3).

2.2 | Description of the scattering problem

The solution u that satisfies the Helmholtz equation (3) is denoted the total wave. By using the scattered and incoming wave components, the total wave is split as $u = u^s + u^i$, where the scattered wave u^s satisfies an outgoing wave condition. Existence and uniqueness of solutions to problem (3) have been shown^{23,24} by using the Lippmann–Schwinger formulation [25, ch. 8] of the problem.

If we let $\Omega_a := B(x_0, r = a)$, then an exact outgoing wave condition can be defined through the use of the Dirichlet-to-Neumann operator $\mathcal{G}(\omega)$ [26, ch. 3] defined for $x \in \Gamma_a := \partial\Omega_a$. Then, the equation for the scattered wave reads

$$\begin{aligned} -\Delta u^s - \omega^2 n^2 u^s &= f, & x \in \Omega_a, \\ \nabla u^s \cdot \mathbf{n} &= \mathcal{G}(\omega) u^s, & x \in \Gamma_a, \end{aligned} \quad (4)$$

where \mathbf{n} is the outward unit vector. For a piecewise constant index of refraction $n \in L^\infty(\Omega_a)$ a dielectric scatterer can be defined as $\Omega_s := \text{supp}(n^2 - 1)$, which is assumed compact within Ω_a . Particularly, we set $n = 1$ for $x \in \Omega_a \setminus \Omega_s$, and $n = n_s \neq 1$ constant for $x \in \Omega_s$. A sketch of the problem is presented in Figure 1.

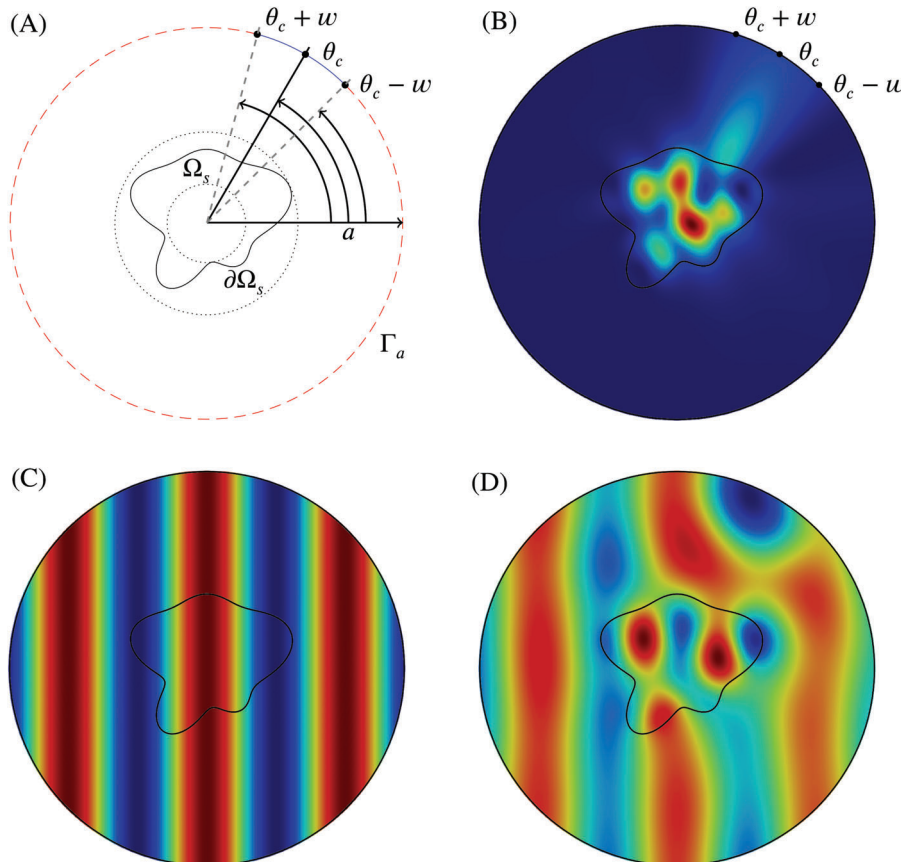


FIGURE 1 Scattering corresponding to the design Ω_s optimized for $\theta_c = 60^\circ$, $w = 15^\circ$, $n_s = 2$, $\omega = 3$, and $N = 5$. In the upper panels, we present (A) a sketch featuring the final design Ω_s and the parametrizations for the box constraints and target angle windows employed in the optimization problem. The corresponding visualization of $|u^s|^2$ is given in (B) with u^s the solution of problem (4). In the lower panels, we present the corresponding visualizations for (C) $\text{Re } u^i$ the incoming wave and (D) $\text{Re } u$ the total wave from the splitting $u := u^s + e^{i\omega x_1}$

In the case of illumination by an incoming plane wave $u^i = e^{i\omega x_1}$, then the source $f \in L^2(\Omega_a)$ is given by $f := \omega^2(n^2 - 1)e^{i\omega x_1}$. The effect of the operator $\mathcal{G}(\omega)$ applied on u^s reads

$$\mathcal{G}(\omega) u^s := \frac{1}{2\pi} \sum_{\nu=-\infty}^{\infty} \omega \frac{H'_\nu(\omega a)}{H_\nu(\omega a)} e^{i\nu\theta} \int_0^{2\pi} u^s(a, \theta') e^{-i\nu\theta'} d\theta', \quad (5)$$

where H_ν is the Hankel function of first kind and order ν .

In practice, an approximation \mathcal{G}^l is used instead of the full series (5), where the accuracy of the FE computation depends critically on the number of terms used in the truncation of the series [26, sec. 3.2.3]. Convergence of FE methods for Helmholtz problems with a truncated DtN map as boundary condition was proven by Melenk.²⁷ Numerical studies for scattering²⁶ and resonance problems¹⁸ suggest that the truncation rule $|\nu| = l > \lceil \omega a \rceil$ results in accurate FE computations.

The implementation of the truncated DtN operator used in this work is based on the implementation by Araújo et al.¹⁸

2.3 | Geometrical description of the scatterers

Consider a smooth *star-shaped* domain $\Omega_s \subset \Omega_a$ as the region contained inside the closed smooth curve $\partial\Omega_s$ as depicted in Figure 1. We restrict our attention to scatterers that deviate from a circle with radius r_m , and can be described by polar coordinates (r, θ) from its center. For this, we introduce a single dielectric scatterer Ω_s with boundary $\partial\Omega_s$, defined by the representation $\mathbf{x} := \mathbf{x}_0 + R(\theta) \cdot [\cos \theta, \sin \theta]^\top$. We only allow designs that are bounded by the annular region defined by the fixed values r_1 and r_2 , as shown in dotted lines in Figure 1. That is, the designs satisfy $0 < r_1 < R(\theta) < r_2 < a$, and we set $r_m := (r_1 + r_2)/2$. In this setting it is natural to use the following Fourier representation of the scatterer

$$R(\theta) = r_m + \sum_{j=1}^N (\alpha_{2j-1} \cos(j\theta) + \alpha_{2j} \sin(j\theta)), \quad (6)$$

from where the parameters $\alpha = (\alpha_1, \dots, \alpha_{2N})^\top$ are chosen as the design variables.

2.4 | Objective function

The so-called Poynting's vector $\mathbf{S} := \mathbf{E} \times \overline{\mathbf{H}}$ specifies the pointwise direction of wave propagation and its magnitude is equivalent to the electromagnetic energy flux. In our setting, and with $u := E_3$, we write for $x \in \Gamma_a$

$$\mathbf{S} := \mathbf{E} \times \overline{\mathbf{H}} = \mathbf{E} \times \overline{\left(\frac{1}{i\omega} \nabla \times \mathbf{E} \right)} = -\frac{1}{i\omega} u \nabla \bar{u}. \quad (7)$$

The energy of the electromagnetic scattered wave leaving Ω_a is proportional to the functional

$$\operatorname{Re} \int_0^{2\pi} \mathbf{S} \cdot \mathbf{n} d\theta = \frac{1}{\omega} \operatorname{Im} \int_0^{2\pi} u \nabla \bar{u} \cdot \mathbf{n} d\theta, \quad (8)$$

where $\mathbf{n} = [\cos \theta, \sin \theta]^\top$ is the outer normal vector to Ω_a . Similarly, the output energy over a window $I_k \subset [0, 2\pi)$ is proportional to

$$J_k(\alpha) := \operatorname{Im} \int_{I_k} u \nabla \bar{u} \cdot \mathbf{n} d\theta = \frac{1}{2i} \int_{I_k} (u \nabla \bar{u} - \bar{u} \nabla u) \cdot \mathbf{n} d\theta, \quad k = 1, 2, \quad (9)$$

where u solves the governing equation (4) for the design/shape defined by α . Then, by letting the target window of length $2w$ centered at the angle θ_c be defined as the interval $I_1 = [\theta_c - w, \theta_c + w]$, and its complement as $I_2 = [0, 2\pi) \setminus I_1$, we introduce the so-called *scattering efficiency* as

$$J(\alpha) := \frac{J_1(\alpha)}{J_2(\alpha)}. \quad (10)$$

Recall that our main objective is to maximize the scattering efficiency.

Feasible designs satisfy the constraints $r_1 < R(\alpha, \theta) < r_2$ for $\theta \in [0, 2\pi)$. The constrained optimization problem is cast as an unconstrained optimization problem by introducing a penalization that increases when $R(\alpha, \theta)$ oscillates away from r_m and grows unbounded as $R(\alpha, \theta)$ tends to r_1 or r_2 . In order to enforce the bound constraints, we introduce the *logarithmic well*

$$J_c(\alpha) := - \int_0^{2\pi} \log |R(\alpha, \theta) - r_1| + \log |r_2 - R(\alpha, \theta)| \, d\theta. \quad (11)$$

Moreover, to promote optimal designs with less oscillatory shapes we use the following penalization term

$$J_p(\alpha) := \int_0^{2\pi} \left(\frac{d^2 R}{d\theta^2} \right)^2 \, d\theta = \pi \sum_{j=1}^N J^4(\alpha_{2j-1}^2 + \alpha_{2j}^2), \quad (12)$$

where we have used the orthogonality of trigonometric functions and representation (6).

We define the objective function as

$$\min_{\alpha} -J(\alpha) + \eta J_c(\alpha) + \gamma J_p(\alpha), \quad (13)$$

for given parameters $\eta, \gamma > 0$.

3 | VARIATIONAL FORMULATION AND DISCRETIZATION

The variational formulation to problem (4) reads: For given $f \in L^2(\Omega_a)$, $\omega \in \mathbb{R}$, and $n \in L^\infty(\Omega_a)$, find $u^s \in H^1(\Omega_a)$ such that

$$\int_{\Omega_a} \nabla u^s \cdot \nabla \bar{v} \, d\mathbf{x} - \omega^2 \int_{\Omega_a} n^2(\mathbf{x}) u^s \bar{v} \, d\mathbf{x} - \int_{\Gamma_a} \mathcal{G}^l(\omega) u^s \bar{v} \, d\mathbf{x} = \int_{\Omega_a} f \bar{v} \, d\mathbf{x}, \quad (14)$$

for all $v \in H^1(\Omega_a)$.

Let the domain $\Omega_a \subset \mathbb{R}^2$ be covered with a regular and quasi-uniform finite element mesh $\mathcal{T}(\Omega_a)$ consisting of N_K quadrilateral elements $\{K_j\}_{j=1}^{N_K}$. The mesh is *shape regular* [28, sec. 4.3] and designed such that n^2 is constant in each K_j . Let h_j be the length of the largest diagonal of the noncurved primitive K_j and denote by h the maximum mesh size $h := \max_j h_j$. Additionally, \mathcal{P}_p denotes the space of polynomials on \mathbb{R}^2 of degree $\leq p$ in each space coordinate. Finally, we define the N_γ dimensional finite element space as

$$V_\gamma(\Omega_a) := \{u \in H^1(\Omega_a) : u|_{K_j} \in \mathcal{P}_p(K_j) \text{ for } K_j \in \mathcal{T}\}. \quad (15)$$

We introduce the shape functions $\{\varphi_j\}_{j=1}^{N_\gamma}$ and the representation $u_h = \sum_{j=1}^{N_\gamma} u_j \varphi_j$, by defining the solution vector $\mathbf{u} := (u_1, u_2, \dots, u_{N_\gamma})^\top$.

To use the exact parametrization of shapes we employ curvilinear elements²⁹ and bend the edges of an initial mesh of good quality. Curved boundaries or interfaces are implemented by using a bilinear transfinite interpolant,^{30,31} where the parametrization of curved edges are available. The use of transfinite interpolation does not guarantee a one-to-one mapping, however, difficult cases due to nonuniqueness seem to appear only in extreme cases that are not experienced in the current project. For reference, computational details and application to FE assembly can be found in the paper by Gordon and Hall³⁰ as well as in the reference book by Solin [32, sec. 3.2].

3.1 | Details on the FE discretization

The outgoing condition is set up by using the definition (5). We compute along the circle Γ_a

$$\begin{aligned} (\mathcal{G}\varphi_j, \varphi_i)_{\Gamma_a} &= \frac{1}{2\pi} \sum_{v=-l}^l \omega \frac{H'_v(\omega a)}{H_v(\omega a)} \int_{\Gamma_a} \bar{\varphi}_i(a, \theta) e^{iv\theta} \int_0^{2\pi} \varphi_j(a, \theta') e^{-iv\theta'} d\theta' ds \\ &= \sum_{v=-l}^l \omega \frac{H'_v(\omega a)}{H_v(\omega a)} \left(\frac{1}{\sqrt{2\pi}} \int_{\Gamma_a} \bar{\varphi}_i e^{iv\theta} ds \right) \left(\frac{1}{a\sqrt{2\pi}} \int_{\Gamma_a} \varphi_j e^{-iv\theta'} ds' \right) \\ &= \sum_{v=-l}^l \omega a \frac{H'_v(\omega a)}{H_v(\omega a)} \hat{\varphi}_j^v \bar{\hat{\varphi}}_i^v, \end{aligned} \quad (16)$$

where we have used $ds' = a d\theta'$ and $\hat{\varphi}_j^v = \frac{1}{a\sqrt{2\pi}} \int_{\Gamma_a} \varphi_j e^{-iv\theta} ds$.

From the variational form (14), we obtain our FE matrices \mathbf{A} , \mathbf{M} , and \mathbf{Q}^v and load vector \mathbf{b} with entries

$$A_{ij} = (\nabla \varphi_j, \nabla \varphi_i)_{\Omega_a}, \quad M_{ij} = (n^2 \varphi_j, \varphi_i)_{\Omega_a}, \quad Q_{ij}^v = \hat{\varphi}_j^v \bar{\hat{\varphi}}_i^v, \quad \text{and} \quad b_i = (f, \varphi_i)_{\Omega_a}, \quad (17)$$

respectively.

The truncated DtN matrix is

$$\mathbf{G}^l(\omega) := \sum_{v=-l}^l \omega a \frac{H'_v(\omega a)}{H_v(\omega a)} \mathbf{Q}^v. \quad (18)$$

The state equation, or discrete scattering problem, becomes

$$\mathbf{S}(\omega) \mathbf{u} := (\mathbf{A} - \omega^2 \mathbf{M} - \mathbf{G}^l(\omega)) \mathbf{u} = \mathbf{b}, \quad (19)$$

with system matrix $\mathbf{S} \in \mathbb{C}^{N_h \times N_h}$ and load vector $\mathbf{b} \in \mathbb{C}^{N_h}$.

In the discrete case, the functional (9) is evaluated as

$$J_k(\boldsymbol{\alpha}) := \frac{1}{2i} \bar{\mathbf{u}}^\top \mathbf{W}_k \mathbf{u}, \quad \text{for } k = 1, 2, \quad (20)$$

with the *antisymmetrical window* matrices

$$\{\mathbf{W}_k\}_{ij} := \int_{I_k} (\varphi_i \nabla \varphi_j - \varphi_j \nabla \varphi_i) \cdot \mathbf{n} d\theta = \int_0^{2\pi} (\varphi_i \nabla \varphi_j - \varphi_j \nabla \varphi_i) \cdot \mathbf{n} \chi_k(\theta) d\theta, \quad \text{for } k = 1, 2, \quad (21)$$

where χ_k is the characteristic function of the interval I_k . In the implementation, we replace χ_k with its mollified version $\tilde{\chi}_k$.

3.2 | Numerical sensitivities

For simplicity of the presentation the derivatives with respect to design variables are referred to as *sensitivities*. The sensitivities for the objective function (13) are

$$\nabla f := \left(\frac{\partial f}{\partial \alpha_1}, \frac{\partial f}{\partial \alpha_2}, \dots, \frac{\partial f}{\partial \alpha_{2N}} \right)^\top, \quad \text{with} \quad \frac{\partial f}{\partial \alpha_j} := -\frac{\partial J}{\partial \alpha_j} + \eta \frac{\partial J_c}{\partial \alpha_j} + \gamma \frac{\partial J_p}{\partial \alpha_j}. \quad (22)$$

The sensitivities corresponding to the penalization terms can be written as follows. For the logarithmic well, we write

$$\frac{\partial J_c}{\partial \alpha_j} = - \int_0^{2\pi} \left(\frac{1}{R(\alpha, \theta) - r_1} - \frac{1}{r_2 - R(\alpha, \theta)} \right) \frac{\partial R}{\partial \alpha_j} d\theta, \quad (23)$$

and for the penalization of oscillatory shapes, we write

$$\frac{\partial J_p}{\partial \alpha_m} = 2\pi j^4 \alpha_m, \quad \text{with } j := \lceil \frac{m}{2} \rceil. \quad (24)$$

Next, we briefly describe how to obtain an exact expression that allow us to compute the sensitivities (22) by using an exact discrete adjoint method [33, sec. 6.2.1]. The state $\mathbf{u}(\alpha)$ solves the system $\mathbf{S}(\alpha)\mathbf{u}(\alpha) = \mathbf{b}(\alpha)$, which allows us to evaluate $J(\alpha)$ using expression (10).

The sensitivities of $J_k(\alpha)$ are written by employing the chain rule for complex valued problems

$$\begin{aligned} \frac{\partial J_k}{\partial \alpha_j} &= \frac{1}{2i} \left((\mathbf{W}_k \mathbf{u})^\top \frac{\partial \mathbf{u}}{\partial \alpha_j} + (\mathbf{W}_k^\top \bar{\mathbf{u}})^\top \frac{\partial \bar{\mathbf{u}}}{\partial \alpha_j} \right) \\ &= \frac{1}{2i} \left((\mathbf{W}_k \mathbf{u})^\top \frac{\partial \mathbf{u}}{\partial \alpha_j} - \overline{(\mathbf{W}_k \mathbf{u})^\top \frac{\partial \mathbf{u}}{\partial \alpha_j}} \right) \\ &= \text{Im} \left\{ (\mathbf{W}_k \mathbf{u})^\top \frac{\partial \mathbf{u}}{\partial \alpha_j} \right\}, \end{aligned} \quad (25)$$

for $k=1, 2$, where we have used the antisymmetric property $\mathbf{W}_k^\top = -\mathbf{W}_k$. By differentiating the state equation (19), we obtain

$$\frac{\partial \mathbf{S}}{\partial \alpha_j} \mathbf{u} + \mathbf{S} \frac{\partial \mathbf{u}}{\partial \alpha_j} = \frac{\partial \mathbf{b}}{\partial \alpha_j}, \quad \text{and define } \mathbf{g} := \frac{\partial \mathbf{b}}{\partial \alpha_j} - \frac{\partial \mathbf{S}}{\partial \alpha_j} \mathbf{u}. \quad (26)$$

Let $\mathbf{D} := c_1 \mathbf{W}_1 - c_2 \mathbf{W}_2$, with constants $c_1 = 1/J_2$, and $c_2 = J_1/J_2^2$. Then, we write the sensitivities of $J(\alpha)$ as

$$\frac{\partial J}{\partial \alpha_j} = \text{Im} \left\{ (\mathbf{D} \mathbf{u})^\top \frac{\partial \mathbf{u}}{\partial \alpha_j} \right\} = \text{Im} \left\{ (\mathbf{D} \mathbf{u})^\top \mathbf{S}^{-1} \mathbf{g} \right\}. \quad (27)$$

In the adjoint method, we define the adjoint vector $\lambda \in \mathbb{C}^{N_r}$ as the solution to the so-called adjoint equation

$$\mathbf{S}^\top \lambda = \mathbf{D} \mathbf{u}. \quad (28)$$

Then, Equations (27) and (28) are combined to obtain

$$\frac{\partial J}{\partial \alpha_j} = \text{Im} \left\{ \lambda^\top \mathbf{g} \right\}. \quad (29)$$

We describe in Section 3.4 how the sensitivities for the system matrix and load vector, used in (29), are computed.

3.3 | Numerical optimization strategy (BFGS)

The chosen numerical optimization strategy, which we describe below, is a variant from the so-called BFGS method,³⁴ where a correction is added in the case when an update leads to an unfeasible design.

Assume that we are at iteration n and let $f_n := f(\alpha_n)$, be the corresponding evaluations of the objective function at each iteration of the optimization scheme, and \mathbf{B}_n be a low rank positive definite approximation to the Hessian matrix $\nabla^2 f(\alpha_n)$. The proposed numerical optimization strategy, as well as standard BFGS, consists in performing the following steps each iteration

$$\mathbf{B}_n \mathbf{p}_n = -\nabla f_n, \quad \alpha_{n+1} = \alpha_n + \mu_n \mathbf{p}_n, \quad (30)$$

where μ_n is the step length in the computed search direction \mathbf{p}_n . The matrix is updated as

$$\mathbf{B}_{n+1} = \mathbf{B}_n - \frac{\mathbf{B}_n \mathbf{s}_n \mathbf{s}_n^\top \mathbf{B}_n}{\mathbf{s}_n^\top \mathbf{B}_n \mathbf{s}_n} + \frac{\mathbf{y}_n \mathbf{y}_n^\top}{\mathbf{y}_n^\top \mathbf{s}_n}, \quad (31)$$

with $\mathbf{s}_n = \boldsymbol{\alpha}_{n+1} - \boldsymbol{\alpha}_n$, $\mathbf{y}_n = \nabla f_{n+1} - \nabla f_n$, and with $\mathbf{B}_0 = \mathbf{I}$ the identity matrix.

To determine the step length μ_n , we apply an inexact line search by using backtracking and require μ_n to satisfy the Armijo condition

$$f(\boldsymbol{\alpha}_n + \mu_n \mathbf{p}_n) \leq f(\boldsymbol{\alpha}_n) + c_1 \mu_n \mathbf{p}_n^\top \nabla f_n \quad \text{for } c_1 > 0. \quad (32)$$

The standard approach is to use as initial guess $\mu_n = 1$ and verify (32). However, in our case this may lead to unfeasible shapes. So, if $r_1 < R(\boldsymbol{\alpha}_n + \mathbf{p}_n, \theta) < r_2 \forall \theta$ we use $\mu_n = 1$ as initial guess, else we set the initial μ_n to the largest constant $c \in (0, 1)$ such that $r_1 < R(\boldsymbol{\alpha}_n + c \mathbf{p}_n, \theta) < r_2$. In our setting the feasibility check is computationally inexpensive compared to solving the governing equation (19). For the Armijo condition (32) we use the recommended³⁴ value $c_1 = 10^{-4}$.

We employ a so-called continuation approach for the logarithmic well parameter η . That is, instead of a single problem we solve for designs in a sequence of problems that approach in each step the original unconstrained problem. Then, in the first stage of the iterative scheme a design is computed from a problem penalized with η_j and it is used as an initial guess for a new problem with η_{j+1} . The starting penalization is chosen as $\eta_0 = 1$, and it is updated as

$$\eta_{j+1} = \eta_j / 2 \quad \text{when} \quad \|\nabla_{\boldsymbol{\alpha}} f\| < \text{TOL}_{\eta}. \quad (33)$$

The updating parameter is chosen as $\text{TOL}_{\eta} = 10^{-2}$, for $\eta_j \geq 10^{-3}$. Then, for $\eta_j < 10^{-3}$ the iterations are stopped once $\|\nabla_{\boldsymbol{\alpha}} f\| < 10^{-5}$.

3.4 | Master element and transfinite interpolation

Let $\mathcal{K} := (-1, 1)^2$ denote the master element, where chart points $\xi \in \mathcal{K}$ are assigned the coordinates $\xi = (\xi, \eta)^\top$. Consider a point $\mathbf{x} = (x, y)^\top$ in a physical element K . Let $X_K : (\xi, \eta) \rightarrow (x, y)$ be the mapping transforming coordinates from the master to physical element. In the case where K is a quadrilateral, the transformation is a simple bilinear mapping. Furthermore, when K has curved edges, then we represent $X_K(\mathcal{K})$ by a bilinear transfinite interpolation.

In the matrix assembly process, integrals over K are mapped to the reference element by using the X_K 's Jacobian matrix \mathbf{J} and its determinant $|\mathbf{J}| = \det \mathbf{J}$ [32, sec. 3.4]. At element K , we have

$$\mathbf{J} := \begin{bmatrix} \frac{\partial X_{K,1}}{\partial \xi} & \frac{\partial X_{K,1}}{\partial \eta} \\ \frac{\partial X_{K,2}}{\partial \xi} & \frac{\partial X_{K,2}}{\partial \eta} \end{bmatrix}, \quad \mathbf{Q} := \begin{bmatrix} \frac{\partial X_{K,2}}{\partial \eta} & -\frac{\partial X_{K,2}}{\partial \xi} \\ -\frac{\partial X_{K,1}}{\partial \eta} & \frac{\partial X_{K,1}}{\partial \xi} \end{bmatrix}, \quad \mathbf{J}^{-1} = \frac{1}{|\mathbf{J}|} \mathbf{Q}, \quad \text{and} \quad |\mathbf{J}| := \det \mathbf{J}. \quad (34)$$

In this setting, integrals transform as

$$\int_K f(\mathbf{x}) \, d\mathbf{x} = \int_{\mathcal{K}} f \circ X_K(\xi) |\mathbf{J}(\xi)| \, d\xi. \quad (35)$$

We denote by φ_j and $\nabla \varphi_j$ the shape functions and shape gradients corresponding to the physical mesh. Similarly, ϕ_j and $\nabla_{\xi} \phi_j$ denote the Lagrange basis functions and gradients corresponding to \mathcal{K} . The assembly of the FE matrices given in Section 3.1 is performed by adding local FE matrices computed at each element. Then, at element K the local stiffness matrix is computed as

$$A_{ij}^K = \int_K \nabla \varphi_j(\mathbf{x}) \cdot \nabla \varphi_i(\mathbf{x}) \, d\mathbf{x} = \int_{\mathcal{K}} \mathbf{J}^{-1} \nabla_{\xi} \phi_j(\xi) \cdot \mathbf{J}^{-1} \nabla_{\xi} \phi_i(\xi) |\mathbf{J}(\xi)| \, d\xi, \quad (36)$$

where we have used the properties $\phi_j(\xi) = \varphi_j \circ X_K(\xi)$ and $\nabla_{\xi} \phi_j = \mathbf{J} \nabla \varphi_j$.

3.4.1 | Explicit computation of sensitivities

In this section, we describe in detail how the sensitivities from the state equation are computed. Let us begin with the local load vector at element K

$$b_i^K = \int_K f(\mathbf{x}) \varphi_i(\mathbf{x}) \, d\mathbf{x} = \int_K f \circ X_K(\xi) \, \phi_i(\xi) \, |\mathbf{J}(\xi)| \, d\xi. \quad (37)$$

We use the following property

$$\frac{\partial}{\partial \alpha_m} f(\mathbf{x}) = \frac{\partial f}{\partial x} \frac{dX_{K,1}}{d\alpha_m} + \frac{\partial f}{\partial y} \frac{dX_{K,2}}{d\alpha_m} = (\nabla f \circ X_K(\xi)) \cdot \frac{\partial}{\partial \alpha_m} X_K(\xi) \quad (38)$$

and compute the sensitivities as

$$\begin{aligned} \frac{\partial b_i^K}{\partial \alpha_m} &= \frac{\partial}{\partial \alpha_m} \int_K f(\mathbf{x}) \varphi_i(\mathbf{x}) \, d\mathbf{x} \\ &= \frac{\partial}{\partial \alpha_m} \int_K f \circ X_K(\xi) \, \phi_i(\xi) \, |\mathbf{J}(\xi)| \, d\xi \\ &= \int_K \frac{\partial}{\partial \alpha_m} (f \circ X_K(\xi) \, |\mathbf{J}(\xi)|) \, \phi_i(\xi) \, d\xi \\ &= \int_K \phi_i(\xi) \left\{ (\nabla f \circ X_K(\xi)) \cdot \frac{\partial}{\partial \alpha_m} X_K(\xi) \, |\mathbf{J}(\xi)| + f \circ X_K(\xi) \frac{\partial |\mathbf{J}|}{\partial \alpha_m} \right\} d\xi. \end{aligned} \quad (39)$$

Similarly, we can compute the sensitivities of the local mass matrix as

$$\frac{\partial M_{ij}^K}{\partial \alpha_m} = \frac{\partial}{\partial \alpha_m} \int_K n_K^2 \varphi_j(\mathbf{x}) \varphi_i(\mathbf{x}) \, d\mathbf{x} = n_K^2 \int_K \phi_j(\xi) \phi_i(\xi) \frac{\partial |\mathbf{J}|}{\partial \alpha_m} \, d\xi, \quad (40)$$

where we have used that $n(\mathbf{x})$ is an elementwise constant function in Ω_a ; that is, $n(\mathbf{x}) \equiv n_K$ for all $\mathbf{x} \in K$.

The computation of the sensitivities of the local stiffness matrix is somewhat more involved as it is illustrated below

$$\begin{aligned} \frac{\partial A_{ij}^K}{\partial \alpha_m} &= \frac{\partial}{\partial \alpha_m} \int_K \nabla \varphi_j(\mathbf{x}) \cdot \nabla \varphi_i(\mathbf{x}) \, d\mathbf{x} \\ &= \frac{\partial}{\partial \alpha_m} \int_K \mathbf{J}^{-1} \nabla_\xi \phi_j(\xi) \cdot \mathbf{J}^{-1} \nabla_\xi \phi_i(\xi) \, |\mathbf{J}(\xi)| \, d\xi \\ &= \frac{\partial}{\partial \alpha_m} \int_K \mathbf{Q} \nabla_\xi \phi_j \cdot \mathbf{Q} \nabla_\xi \phi_i \frac{1}{|\mathbf{J}(\xi)|} \, d\xi \\ &= \frac{\partial}{\partial \alpha_m} \int_K (\nabla_\xi \phi_j)^\top \mathbf{Q}^\top \mathbf{Q} \nabla_\xi \phi_i \frac{1}{|\mathbf{J}(\xi)|} \, d\xi \\ &= \int_K (\nabla_\xi \phi_j)^\top \left(\frac{\partial \mathbf{Q}^\top}{\partial \alpha_m} \mathbf{Q} + \mathbf{Q}^\top \frac{\partial \mathbf{Q}}{\partial \alpha_m} - \frac{1}{|\mathbf{J}(\xi)|} \frac{\partial |\mathbf{J}(\xi)|}{\partial \alpha_m} \mathbf{Q}^\top \mathbf{Q} \right) \nabla_\xi \phi_i \frac{1}{|\mathbf{J}(\xi)|} \, d\xi. \end{aligned} \quad (41)$$

Finally, after *local-to-global* assembly, the sensitivities of the system matrix read

$$\frac{\partial \mathbf{S}}{\partial \alpha_m} = \frac{\partial \mathbf{A}}{\partial \alpha_m} - \omega^2 \frac{\partial \mathbf{M}}{\partial \alpha_m}. \quad (42)$$

Remark 1. The cells containing edges on the boundary Γ_a are curved by using the mapping X_K . However, the bending is fixed following the circle Γ_a and does not depend on the design variables α . This implies that the DtN representation and window matrices \mathbf{W}_k are not sensitive to variations of the shape. That is, for any m the following holds

$$\frac{\partial \mathbf{G}^l(\omega)}{\partial \alpha_m} \equiv 0 \quad \text{and} \quad \frac{\partial \mathbf{W}_k}{\partial \alpha_m} \equiv 0 \quad \text{for } k = 1, 2. \quad (43)$$

Remark 2. In a numerical optimization strategy, Remark 1 implies that the matrices \mathbf{G}^l and \mathbf{W}_k only need to be assembled once and should not be updated in the iterative scheme. Additionally, the assembly of the sensitivities (42) may be performed only over cells that have an edge belonging to the shape Ω_s . For this, at the creation of the triangulation $\mathcal{T}(\Omega_a)$, we label cells according to their corresponding domain.

3.4.2 | Sensitivities of the Jacobian matrix

To derive the sensitivities of the local FE matrices, we need to delve into the details of the mapping X_K . Here, we consider the physical (quadrilateral) element K with primitive edges e_1, \dots, e_4 and vertices $\mathbf{x}_1, \dots, \mathbf{x}_4$. Curved scatterers are represented on a FE cell K by enforcing its edges to follow smooth curves. These are defined by the parametrizations $X^{e_1}(\xi), \dots, X^{e_4}(\xi) \subset \mathbb{R}^2$, $\xi \in [-1, 1]$. More precisely, the vector valued bilinear transfinite interpolation formula is given by

$$\begin{aligned} X_K(\xi) &:= \begin{pmatrix} X_{K,1}(\xi) \\ X_{K,2}(\xi) \end{pmatrix} \\ &= \frac{1-\xi}{2} X^{e_1}(\eta) + \frac{1+\xi}{2} X^{e_2}(\eta) + \frac{1-\eta}{2} X^{e_3}(\xi) + \frac{1+\eta}{2} X^{e_4}(\xi) \\ &\quad - \frac{(1-\xi)(1-\eta)}{2} \mathbf{x}_1 - \frac{(1-\xi)(1+\eta)}{2} \mathbf{x}_4 \\ &\quad - \frac{(1+\xi)(1-\eta)}{2} \mathbf{x}_2 - \frac{(1+\xi)(1+\eta)}{2} \mathbf{x}_3, \end{aligned} \quad (44)$$

satisfying $X_K(-1, -1) = \mathbf{x}_1$, $X_K(1, -1) = \mathbf{x}_2$, $X_K(1, 1) = \mathbf{x}_3$, $X_K(-1, 1) = \mathbf{x}_4$ (see References 30,31 and [32, sec. 3.3]). This is, at corners the mapping X_K corresponds to the value of the physical nodes.

In the blended formula (44), the parametrizations X^{e_1}, \dots, X^{e_4} are explicit functions of the design variables α , so that X_K has an explicit form depending on ξ, η , and α . In order to compute the Jacobian matrix \mathbf{J} , we need the following derivatives

$$\begin{aligned} \frac{\partial X_K}{\partial \xi} &= -\frac{1}{2} X^{e_1}(\eta) + \frac{1}{2} X^{e_2}(\eta) + \frac{1-\eta}{2} \frac{\partial X^{e_3}}{\partial \xi} + \frac{1+\eta}{2} \frac{\partial X^{e_4}}{\partial \xi} \\ &\quad + \frac{1}{4} [(1-\eta)(\mathbf{x}_1 - \mathbf{x}_2) + (1+\eta)(\mathbf{x}_4 - \mathbf{x}_3)], \end{aligned} \quad (45)$$

and

$$\begin{aligned} \frac{\partial X_K}{\partial \eta} &= \frac{1-\xi}{2} \frac{\partial X^{e_1}}{\partial \eta} + \frac{1+\xi}{2} \frac{\partial X^{e_2}}{\partial \eta} - \frac{1}{2} X^{e_3}(\xi) + \frac{1}{2} X^{e_4}(\xi) \\ &\quad + \frac{1}{4} [(1-\xi)(\mathbf{x}_1 - \mathbf{x}_4) + (1+\xi)(\mathbf{x}_2 - \mathbf{x}_3)]. \end{aligned} \quad (46)$$

Finally, as described in Section 3.4.1, we obtain exact sensitivities for the FE matrices and vectors by computing

$$\frac{\partial \mathbf{J}}{\partial \alpha_m} \quad \text{and} \quad \frac{\partial |\mathbf{J}|}{\partial \alpha_m}, \quad \text{which require} \quad \frac{\partial}{\partial \alpha_m} \left(\frac{\partial X_K}{\partial \xi} \right), \quad \text{and} \quad \frac{\partial}{\partial \alpha_m} \left(\frac{\partial X_K}{\partial \eta} \right). \quad (47)$$

3.4.3 | Parametrization and sensitivities of the curved interface

In this subsection, we describe how to obtain the sensitivities (47) needed for the assembly of local matrices in the master element. We show how to take advantage of the fact that the transfinite interpolation formula (44) is explicit. This allows for the straightforward differentiation with respect to the design variables once the parametrizations $X^{e_1}(\alpha), \dots, X^{e_4}(\alpha)$ are known. The sensitivities (47) of the Jacobian matrix and its determinant (34), require the assembly of each term in the Equations (45) and (46).

For convenience, we sketch in Figure 2 the situation where an element K with vertices $\mathbf{x}_1, \dots, \mathbf{x}_4$ is bent following a shape represented by X^{e_1} . In this case, the vertices $\mathbf{x}_1 = (x_1, y_1)^\top$ and $\mathbf{x}_2 = (x_2, y_2)^\top$ are constrained to follow the shape described by α . In the primitive edge (before bending) we have the interpolated points

$$\begin{bmatrix} x \\ y \end{bmatrix} = X_p(\zeta) = \frac{(1-\zeta)}{2} \begin{bmatrix} x_1 \\ y_1 \end{bmatrix} + \frac{(1+\zeta)}{2} \begin{bmatrix} x_2 \\ y_2 \end{bmatrix}, \quad (48)$$

with $-1 \leq \zeta \leq 1$. Furthermore, since we represent shapes in polar coordinates, we introduce

$$\theta(x, y) := \text{angle}(x, y) \quad \text{with derivative} \quad \frac{d\theta}{d\zeta} = \frac{\partial\theta}{\partial x} \frac{dx}{d\zeta} + \frac{\partial\theta}{\partial y} \frac{dy}{d\zeta}, \quad (49)$$

from where it is obtained

$$\frac{d\theta}{d\zeta} = \frac{1}{2(x^2 + y^2)} (x \cdot (y_2 - y_1) - y \cdot (x_2 - x_1)). \quad (50)$$

$=: g(x, y) \qquad \qquad \qquad =: h(x, y)$

For simplicity of the presentation in the following derivations, we have introduced the functions h and g in formula (50). For the bending function, we employ the shape representation corresponding to the face of K that follows the shape

$$X^e(\zeta) := \begin{bmatrix} x_0 \\ y_0 \end{bmatrix} + R(\theta) \begin{bmatrix} \cos \theta \\ \sin \theta \end{bmatrix}. \quad (51)$$

As described in Section 3.4.1, we make use of the Jacobian matrix and its determinant (34) to map integrals into the reference element \mathcal{K} . In our implementation, we have used θ as the global parameter describing our shapes. In turn, all local vertices and edges attached to the shape depend on θ and also do the sensitivities. Then, differentiation is performed by using the chain rule, which will be employed several times below.

We move forward by observing that expressions (45) and (46) for the derivatives of the transfinite interpolation formula (44) require knowledge of the first-order derivatives of the parametrization X^e with respect to ξ and η . These can be obtained by using the chain rule

$$\frac{\partial X^e}{\partial \zeta} = \frac{\partial X^e}{\partial \theta} \cdot \frac{d\theta}{d\zeta}, \quad \text{with} \quad \frac{\partial X^e}{\partial \theta} = \left(\frac{\partial R}{\partial \theta} \begin{bmatrix} \cos \theta \\ \sin \theta \end{bmatrix} + R(\theta) \begin{bmatrix} -\sin \theta \\ \cos \theta \end{bmatrix} \right), \quad (52)$$

where $\zeta = \xi$ or $\zeta = \eta$.

The evaluation of the sensitivities of the Jacobian matrix (34) require that we have available explicit formulas for $\partial_{\alpha_m}(\partial X^e / \partial \zeta)$. For obtaining these, we notice that points on the curved edge are sensitive to changes of the shape

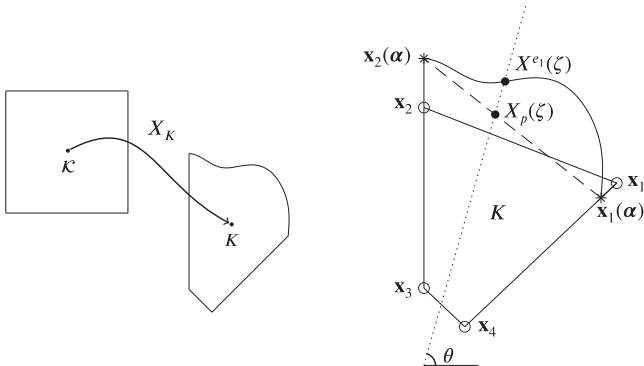


FIGURE 2 Illustration of (left) the action of the mapping $X_K : \mathcal{K} \rightarrow K$ and (right) the corresponding parametrization used for representing the bending of the edge that belongs to the shape $\partial\Omega_s(\alpha)$

parametrization

$$\frac{\partial X^e}{\partial \alpha_m} = \frac{\partial R}{\partial \alpha_m} \begin{bmatrix} \cos \theta \\ \sin \theta \end{bmatrix} + \frac{\partial X^e}{\partial \theta} \frac{\partial \theta}{\partial \alpha_m}. \quad (53)$$

Then, we use the chain rule and obtain

$$\begin{aligned} \frac{\partial}{\partial \alpha_m} \left(\frac{\partial X^e}{\partial \zeta} \right) &= \frac{\partial}{\partial \alpha_m} \left(\frac{\partial X^e}{\partial \theta} \frac{\partial \theta}{\partial \zeta} \right) = \frac{\partial}{\partial \alpha_m} \left(\frac{\partial X^e}{\partial \theta} \right) \frac{\partial \theta}{\partial \zeta} + \frac{\partial X^e}{\partial \theta} \frac{\partial}{\partial \alpha_m} \left(\frac{\partial \theta}{\partial \zeta} \right) \\ &= \left(\frac{\partial}{\partial \alpha_m} \frac{\partial X^e}{\partial \theta} + \frac{\partial^2 X^e}{\partial \theta^2} \frac{\partial \theta}{\partial \alpha_m} \right) \frac{\partial \theta}{\partial \zeta} + \frac{\partial X^e}{\partial \theta} \frac{\partial}{\partial \alpha_m} \left(\frac{\partial \theta}{\partial \zeta} \right), \end{aligned} \quad (54)$$

where we can compute directly

$$\frac{\partial}{\partial \alpha_m} \frac{\partial X^e}{\partial \theta} = \frac{\partial}{\partial \alpha_m} \left(\frac{\partial R}{\partial \theta} \right) \begin{bmatrix} \cos \theta \\ \sin \theta \end{bmatrix} + \frac{\partial R}{\partial \alpha_m} \begin{bmatrix} -\sin \theta \\ \cos \theta \end{bmatrix}, \quad (55)$$

and

$$\frac{\partial^2 X^e}{\partial \theta^2} = \left(\frac{\partial^2 R}{\partial \theta^2} - R \right) \begin{bmatrix} \cos \theta \\ \sin \theta \end{bmatrix} + 2 \frac{\partial R}{\partial \theta} \begin{bmatrix} -\sin \theta \\ \cos \theta \end{bmatrix}. \quad (56)$$

Additionally, we have

$$\frac{\partial \theta}{\partial \alpha_m} = \frac{1}{x^2 + y^2} \left(x \frac{\partial y}{\partial \alpha_m} - y \frac{\partial x}{\partial \alpha_m} \right), \quad (57)$$

and we differentiate the projection formula (48) in order to obtain

$$\frac{\partial x}{\partial \alpha_m} = \frac{(1 - \zeta)}{2} \frac{\partial x_1}{\partial \alpha_m} + \frac{(1 + \zeta)}{2} \frac{\partial x_2}{\partial \alpha_m} \quad \text{and} \quad \frac{\partial y}{\partial \alpha_m} = \frac{(1 - \zeta)}{2} \frac{\partial y_1}{\partial \alpha_m} + \frac{(1 + \zeta)}{2} \frac{\partial y_2}{\partial \alpha_m}. \quad (58)$$

Finally, by using the definitions introduced in formula (49), the sensitivities of the remaining terms in Equation (54) are computed as follows

$$\frac{\partial}{\partial \alpha_m} \left(\frac{\partial \theta}{\partial \xi} \right) = \frac{\partial g}{\partial \alpha_m} h + g \frac{\partial h}{\partial \alpha_m} = \left(\frac{\partial g}{\partial x} \frac{\partial x}{\partial \alpha_m} + \frac{\partial g}{\partial y} \frac{\partial y}{\partial \alpha_m} \right) h + g \frac{\partial h}{\partial \alpha_m}, \quad (59)$$

where

$$\frac{\partial g}{\partial x} = \frac{-x}{(x^2 + y^2)^2}, \quad \text{and} \quad \frac{\partial g}{\partial y} = \frac{-y}{(x^2 + y^2)^2}, \quad (60)$$

and

$$\frac{\partial h}{\partial \alpha_m} = \frac{\partial x}{\partial \alpha_m} (y_2 - y_1) + x \cdot \left(\frac{\partial y_2}{\partial \alpha_m} - \frac{\partial y_1}{\partial \alpha_m} \right) - \frac{\partial y}{\partial \alpha_m} (x_2 - x_1) - y \cdot \left(\frac{\partial x_2}{\partial \alpha_m} - \frac{\partial x_1}{\partial \alpha_m} \right). \quad (61)$$

In this section we have derived all the necessary information required in the formulas for the sensitivities (47) of the Jacobian matrix (34). Particularly, we have given explicit expressions for all terms required in the formulas (53) and (54), which in turn, give formulas for the explicit computation of the sensitivities of the local system matrix and local load vector as described in Section 3.4.1.

3.5 | FE approximation properties and error estimation

Studies for the convergence of the error for Helmholtz problems indicate that the accuracy of a FE approximation deteriorates with increasing wave number k , and that the use of high polynomial order is advantageous to reduce this pollution effect.^{26,35,36} Additionally, for uniform mesh size h and polynomial order p , it has been shown that under sufficient regularity assumptions the conditions $p \approx \log(k)$ and $kh/p < 1$ ensure quasi-optimality of the Galerkin method.³⁷

The derivation of reliable error estimates can be done thoroughly for one-dimensional Helmholtz problems,³⁶ but this is a difficult task for higher dimensions. Nonetheless, it is still possible to draw a sufficiently accurate picture of the behavior of FE approximation for the two-dimensional problem that will suffice for the purpose of the current work.

3.5.1 | FE preasymptotic error estimation

Initially, we estimate the requirements for quasi-optimality of our FE discretization individually on each cell in our triangulation. The refractive index is a piecewise constant function, such that it has maximum magnitude in cells defining Ω_s . The spatial frequency of oscillation of solutions is quantified by the wavenumber $k = |n_s|\omega$. Then, the error for a polynomial approximation is expected to be worse in cells with high wavenumber.

From Melenk and Sauter's results,³⁷ we require the condition

$$\left(\frac{\omega|n_s|h}{\sigma p}\right)^p < 1, \quad \text{for a given constant } \sigma > 0, \quad (62)$$

in order to have sufficiently small pollution in the FE solution. From where we obtain the criterion $p > [\omega|n_s|h/\sigma]$.

3.5.2 | Error estimation for the shape representation

For a fixed mesh size h , as the number of Fourier terms N increases, it is expected that a higher polynomial degree is needed in order to obtain an accurate FE solution. Since each component of our Fourier representation (6) satisfies a one-dimensional Helmholtz equation with periodic boundary conditions, we can reach useful estimates by assuming that we work in the polar plane (r, θ) . We define a polynomial approximation z_h and let $\rho = 2\pi/N_e$, with N_e the number of FE edges that define $\partial\Omega_s$. Then, we can estimate for the highest frequency $j = N$ the FE requirements for the decay of the error $\|z - z_h\|$ in the preasymptotic regime. Following this motivation, we use standard preasymptotic FE error estimation [26, sec. 4.7.6] corresponding to one-dimensional wave problems and obtain

$$\left(\frac{N\rho}{2p}\right)^p < 1, \quad (63)$$

which tells us that the FE pollution effect is small provided that the maximum allowed number of Fourier terms is bounded by $N < \lfloor 2p/\rho \rfloor$. The FE triangulation used for this project features $\rho = 2\pi/8$, from where estimate (63) gives $N < \lfloor 8p/\pi \rfloor$.

Finally, the estimates (62) and (63) indicate that for keeping the relative error fixed, then the computational effort is increased as we require larger values for ω , n_s , and N .

Remark 3. It is possible to improve the performance of the numerical optimization scheme and to lessen the memory requirements by implementing meshes designed a priori by using different FE approximation properties depending on the refractive index function. The outcome of the strategy is to shorten the preasymptotic phase of the FE error for Helmholtz problems with constant coefficients as described in Araújo et al.¹⁹ For clarity of the exposition, and simplicity of the proposed numerical optimization strategy we do not incorporate these ideas in the current work.

4 | IMPLEMENTATION AND VERIFICATION DETAILS

In the remaining of the document, we describe how we set up our implementation and how we implement the ideas described above. Particularly, we start by performing a convergence study on the polynomial order used for the FE discretization. Consecutively, we move on to describing the results of the numerical optimization for the different test cases.

4.1 | Convergence of the discretization error

In the current work, optimal shapes Ω_s are obtained from the model (4) by the solution of the discrete state equation (19) and the sensitivity analysis outlined in Section 3.2 by using the results in Section 3.4.1. These designs are optimal with respect to the model presented in Section 2.2 and depend on the given frequency ω , refractive index n_s , target angle θ_c and number N of Fourier terms.

Following the discussion in Section 3.5.2, we can set up the polynomial order in the FE discretization by performing a study on the FE error convergence for fixed h . First, we select $n_s = 2$ and generate an arbitrary shape consisting of $N = 10$ in representation (6). Consecutively, we fix ω and for a sequence of FE discretizations we vary the polynomial order as $p = 4, 5, \dots, 35$. For each p we compute the values $s(p) = \mathbf{u}^H \mathbf{G}^l \mathbf{u}$. Then, we compare convergence of $s(p)$ by taking $s(35)$ as a reference value and define the relative error

$$E(p) := \left| \frac{s(p) - s(35)}{s(35)} \right|. \quad (64)$$

The results for frequencies $\omega = 3, 5$, and 8 are plotted in Figure 3, where it is confirmed that the relative error increases with frequency. Particularly, the relative error for $p = 20$ is of the order 10^{-10} for $\omega = 3$ and 10^{-9} for $\omega = 5$.

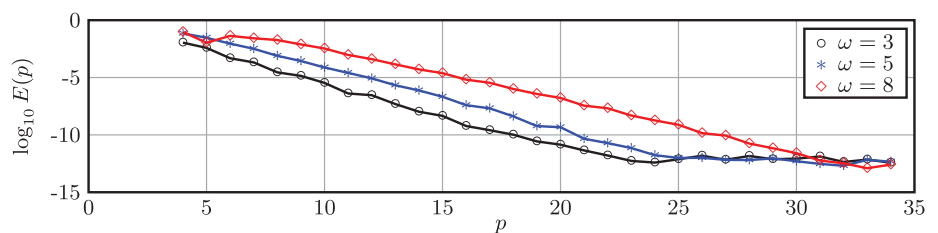
4.2 | Verification against alternative FE software and outgoing condition

The FE discretization employed in the optimization strategy consists of using a high polynomial degree ($p = 20$), a small number of quadrilateral FE cells ($N_K = 28$), and as an outgoing condition we use an accurate DtN map with truncation parameter $l = \lceil 2\omega a \rceil$. Furthermore curvilinear cell edges are used in the representation of the scatterer Ω_s . The implementation is developed by using the FE library `deal.II`³⁸ and linear algebra package `PETSc`.³⁹

To verify the efficiency of resulting optimal designs, we use an alternative FE discretization of the model equation (4), which is implemented in the well-established FE software `NGSolve`.⁴⁰ The discretization used for the verification consists of a low polynomial order ($p = 2$), a large number of triangular cells ($N_K \approx 350,000$) and as outgoing condition we use an out-of-the box radial PML attached at $r = a$, featuring thickness $\ell = 1$, and strength $\sigma_0 = 1$.⁴¹ Additionally, in the verification code, the edges of the dielectric shape Ω_s are linearly interpolated between the vertices defining the shape on the triangular mesh.

We note that the purpose of the comparison is to verify in the eye-ball norm that the scattering efficiencies predicted by our implementation are easily reproduced by a standard FE implementation.

FIGURE 3 Convergence of $E(p)$ with respect to polynomial degree p as described in Section 4.1. For the study we use a shape with $N = 10$, we fix $n_s = 2$ and perform the computations for frequencies $\omega = 3, 5$, and 8



5 | RESULTS

In this section, we describe the numerical computations performed with our implementation and highlight several observations. In all test cases, $w = 15^\circ$ is used as the half-width window; the box constraints have the fixed values $r_1 = 0.6$ and $r_2 = 1.4$, so $r_m = 1$. Unless otherwise stated, we employ $N = 10$ for the Fourier representation (6) and penalize oscillatory designs by setting $\gamma = 10^{-2}$. Finally, the initial design is set to $\alpha_j = 0$ for $j = 1, 2, \dots, 2N$, and the initial logarithmic well penalization parameter is set to $\eta_0 = 1$.

Optimal designs are drawn with a solid line for each test case and the box constraints are dotted. Next to each optimal design we present its corresponding normalized *scattering pattern* as a plot depicting $|\mathbf{S} \cdot \mathbf{n}|$ over Γ_a .

Convergence of the optimization strategy: Figure 4 illustrates a typical convergence of the proposed numerical optimization scheme. From left to right we show plots for a) the resulting optimal designs, b) the corresponding final scattering patterns, and c) iteration history for $f(\alpha)$ drawn with blue stars and $\log \|\nabla_\alpha f\|$ drawn with red circles. The upper panels show results for the target center angle $\theta_c = 60^\circ$ and refractive index $n_s = 2$, and the lower panels for $\theta_c = 120^\circ$ and $n_s = 3$.

The converged optimal designs are very efficient as can be seen from their corresponding scattering patterns. These feature a main peak centered in θ_c of width fitting the target window $I_1 := [\theta_c - w, \theta_c + w]$. Additionally, the optimal designs display a relatively small-scale scattering pattern over $I_2 := [0, 2\pi) \setminus I_1$. From the history plots, we observe the convergence of the numerical optimization strategy. Particularly, the echelon pattern reveals the effect of the dynamic logarithmic well penalization from formula (11). As described in Section 3.3, in the first stage of the iterative scheme we set $\eta_0 = 1$ and update $\eta_{j+1} = \eta_j/2$ when $\|\nabla_\alpha f\| < 10^{-2}$. The second stage starts once $\eta < 10^{-3}$, then iterations are stopped after $\|\nabla_\alpha f\| < 10^{-5}$ is reached.

The case for $\theta_c = 120^\circ$ and $n_s = 3$ requires a larger number of iterations for reaching convergence of the numerical scheme compared to $\theta_c = 60^\circ$ and $n_s = 2$, implying that the former case is a challenging problem.

Influence of the number of Fourier terms: The discussion is moved forward by taking into account the influence of the number of Fourier terms employed for the representation of the optimal designs. Therefore, for the case $\theta_c = 60^\circ$ and $n_s = 2$, we show in Figure 5 a sequence of optimal shapes computed with $N = 1, 2, \dots, 8$. It is observed that as N increases, the resulting designs exhibit larger values for the scattering efficiencies $J(\alpha)$. Optimal designs with lower N (1 and 2) feature scattering patterns with large peaks outside the window I_1 . Increasing N results in scattering patterns that converge to a pattern having a main peak confined within I_1 . Notice that for $N > 4$ the main modifications in the resulting optimal shapes take place near the inner constraint.

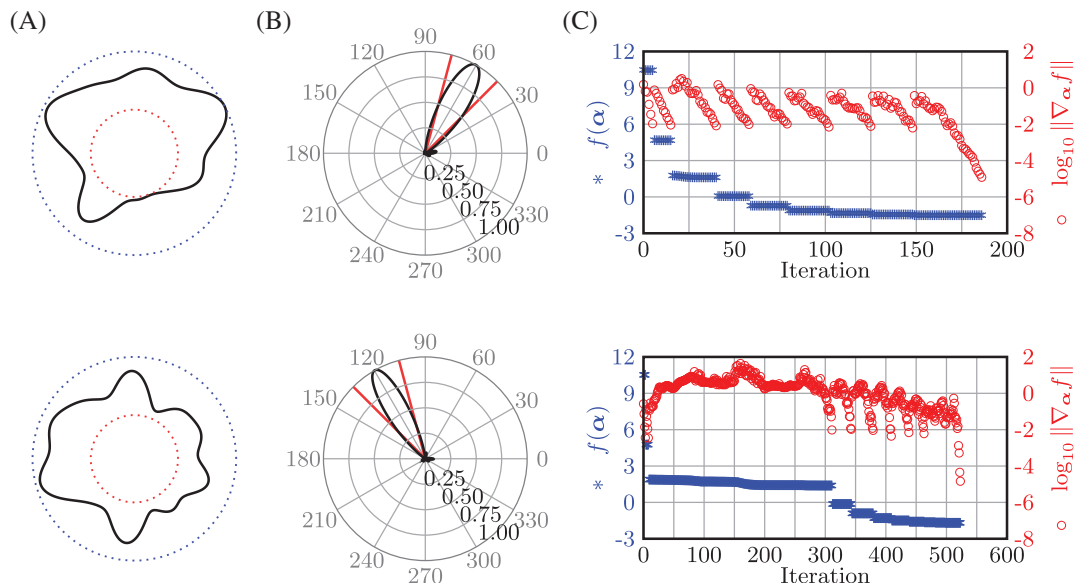


FIGURE 4 Convergence of the numerical optimization scheme: In the upper panels we show results for $\theta_c = 60^\circ$, $n_s = 2$, $N = 10$ and in the lower panels we show results for $\theta_c = 120^\circ$, $n_s = 3$, $N = 10$. From left to right we present (A) optimal designs, (B) scattering patterns, and (C) history of $f(\alpha)$, $\log_{10} \|\nabla_\alpha f\|$ versus iteration

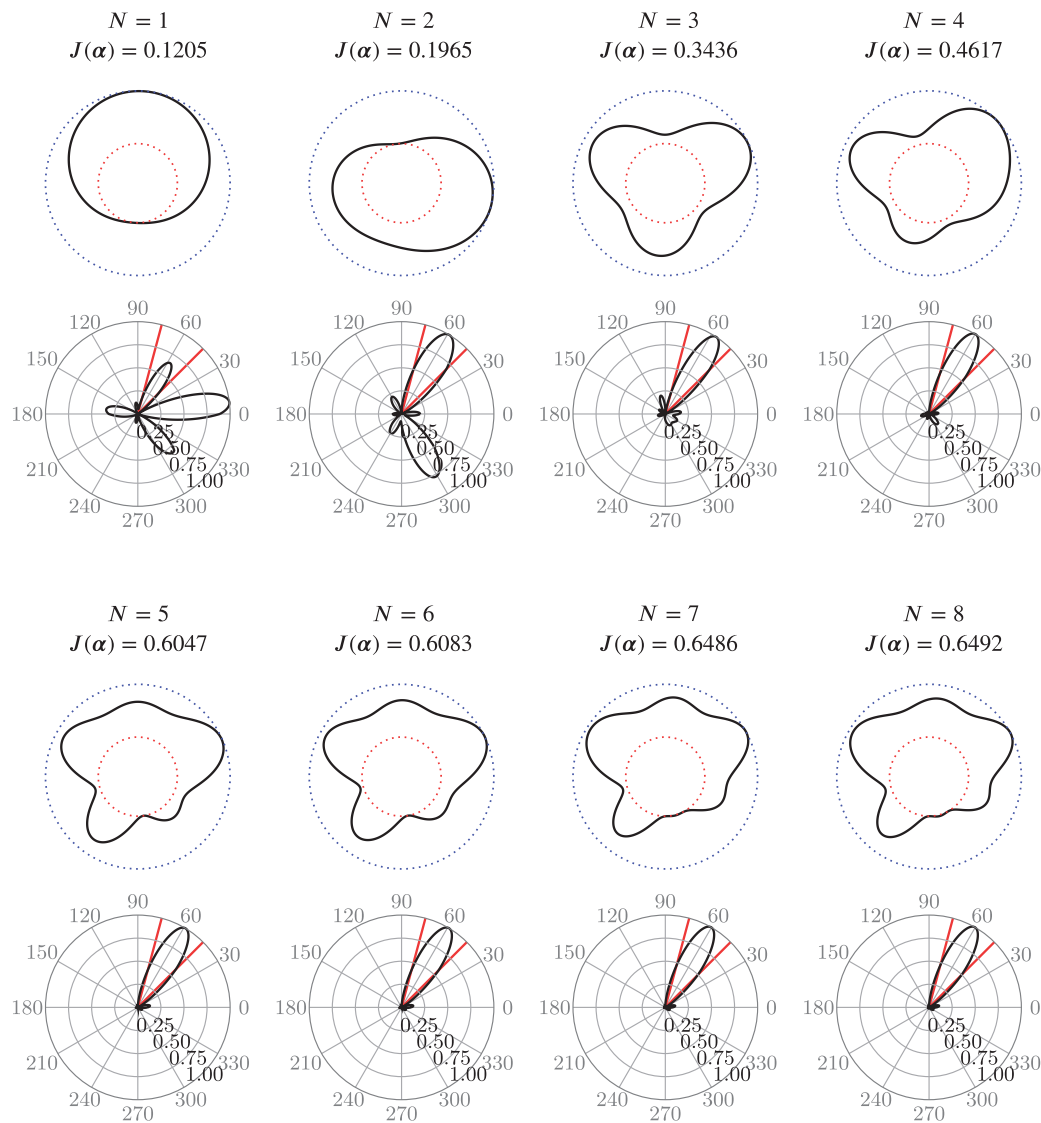


FIGURE 5 Comparison with respect to number of Fourier terms N for fixed $n_s = 2$ and $\theta_c = 60^\circ$. For $N = 1, 2, \dots, 8$, we show optimal designs in the upper panel and scattering patterns in the lower panel

In panel (B) of Figure 1 we plot $|u|^2$ from the solution to the scattering problem (4) for an design optimized for $\theta_c = 60^\circ$, $\omega = 3$, $n_s = 2$, and $N = 5$. The plot features large values inside the scatterer Ω_s and a beam of amplitude that extends from the scatterer to Γ_a . On the boundary Γ_a , it is appreciated that $|u|^2$ resembles the scattering pattern presented in Figure 5 for $N = 5$. This is, a relatively large amplitude is observed within $\theta \in [\theta_c - w, \theta_c + w]$ and almost zero amplitude elsewhere.

For reference, we give below the parametrization for the shape optimized for $\theta_c = 60^\circ$, $\omega = 3$, $n_s = 2$, and $N = 5$. The resulting parametrization α from the representation (6) is

$$\begin{aligned} \alpha_1 &= 0.0140864, & \alpha_2 &= 0.204636, & \alpha_3 &= 0.0409673, & \alpha_4 &= 0.0760092, & \alpha_5 &= 0.0953527, \\ \alpha_6 &= 0.0961718, & \alpha_7 &= -0.0692833, & \alpha_8 &= -0.0383743, & \alpha_9 &= -0.006564, & \alpha_{10} &= 0.136563. \end{aligned}$$

Comparison with respect to target angle: Next, we present optimal designs computed with different target angles $\theta_c = 30^\circ, 60^\circ, 90^\circ$, and 120° . The normalized scattering patterns corresponding to optimal designs are shown by using a solid black line. These results are verified following the description given in Section 4.2 and we add in all plots the verified pattern by using a dashed blue line. Both scattering patterns are normalized with the same constant corresponding to the maximum value at the peak of the black line.

The resulting optimal designs and their respective scattering patterns are presented in Figure 6 for fixed $n_s = 2$ and $\omega = 3$. We observe from the figure that scattering patterns optimized for different target angles exhibit remarkable directional scattering properties. Numerical computations indicate that for low refractive indexes it is easier to reach optimal designs for $\theta_c < 90^\circ$ compared with designs optimized for $\theta_c \geq 90^\circ$. In order to obtain designs with similar scattering efficiencies, we experienced that problems with $\theta_c \geq 90^\circ$ require finer shape representations compared with shapes optimized for $\theta_c < 90^\circ$. Therefore, in Figure 6, the designs corresponding to $\theta_c = 30^\circ$ and 60° were computed with $N = 10$, and the designs corresponding to $\theta_c = 90^\circ$ and 120° were computed with $N = 15$.

Comparison with respect to refractive index: To discuss the difference from optimal designs computed with different refractive indexes n_s , we present in Figure 7 results optimized for $n_s = 3$, $\omega = 3$, and $N = 10$. Comparing the results in Figure 6 with those in Figure 7, we observe that designs optimized for a higher refractive index appear to be more efficient at reducing the scattering amplitudes outside the target window. Additionally, it can be seen that designs optimized with lower n_s occupy a large feasible region and feature boundaries that are very close to the constraints. The results suggest that using a high refractive index is an effective strategy for obtaining efficient designs even for the most challenging cases with $\theta_c \geq 90^\circ$. Finally, we mention that the number of iterations for obtaining a converged design when using high contrast is larger than when using lower contrast.

Comparison with respect to frequency: The last set of optimal designs is gathered in Figure 8, corresponding to scatterers optimized for the frequency $\omega = 5$ and with a fixed refractive index $n_s = 2$. As well as in Figure 6, the designs corresponding to $\theta_c = 30^\circ$ and 60° were computed with $N = 10$, and the designs corresponding to $\theta_c = 90^\circ$ and 120° were

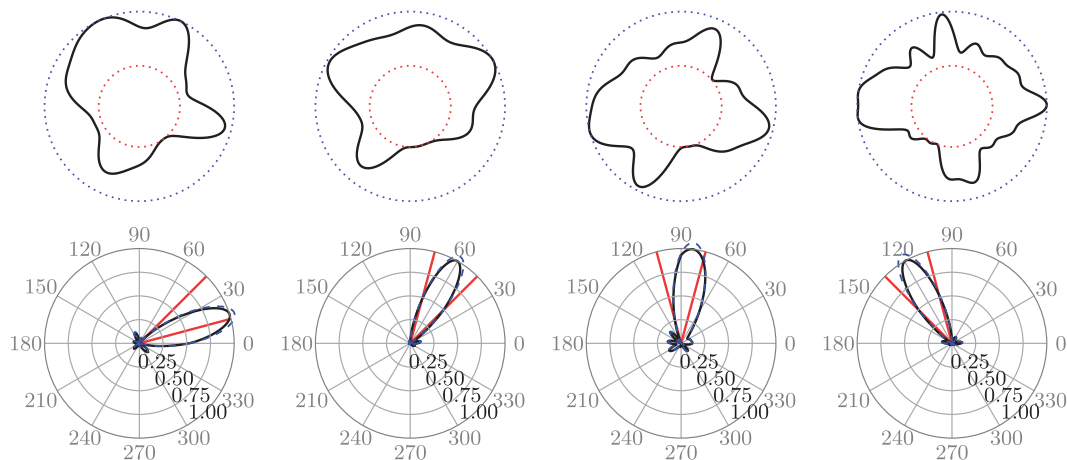


FIGURE 6 Comparison with respect to θ_c for a fixed frequency $\omega = 3$ and refractive index $n_s = 2$

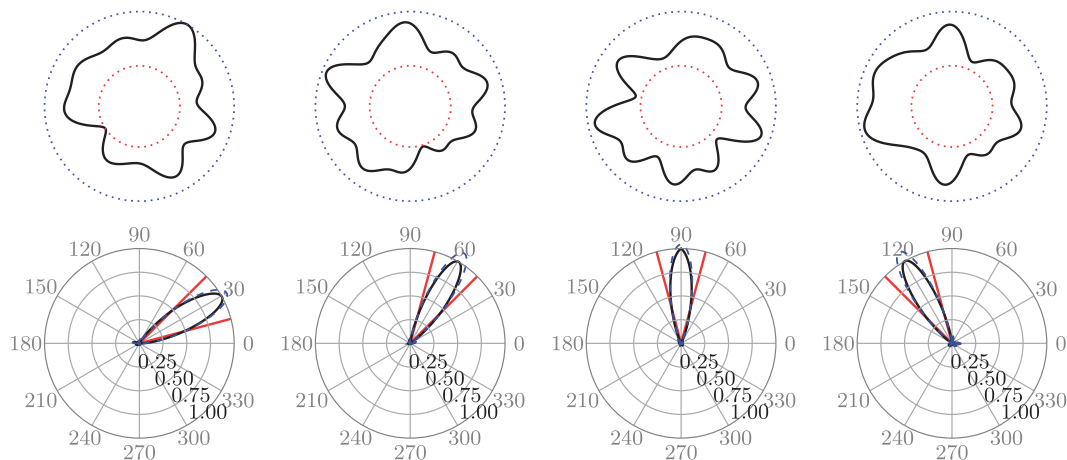


FIGURE 7 Comparison with respect to θ_c for a fixed frequency $\omega = 3$ and refractive index $n_s = 3$

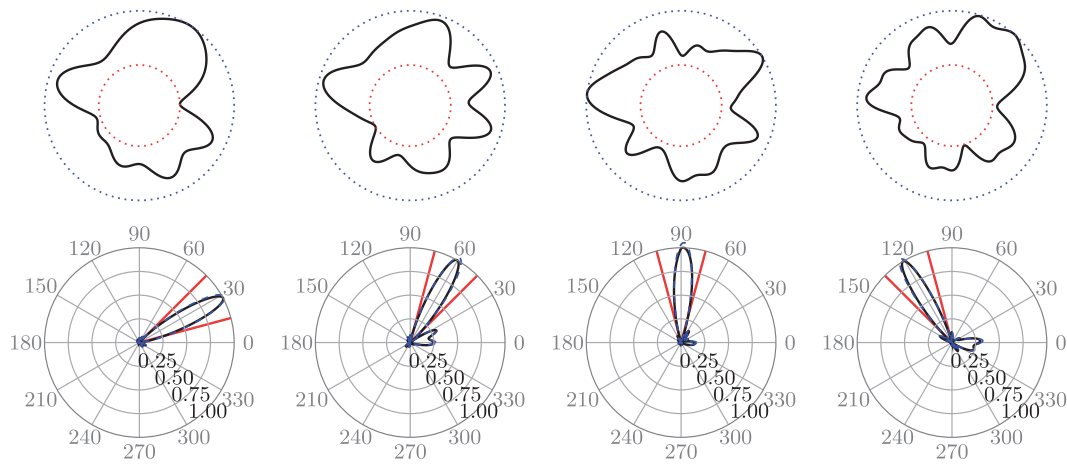


FIGURE 8 Comparison with respect to θ_c for a fixed frequency $\omega = 5$ and refractive index $n_s = 2$

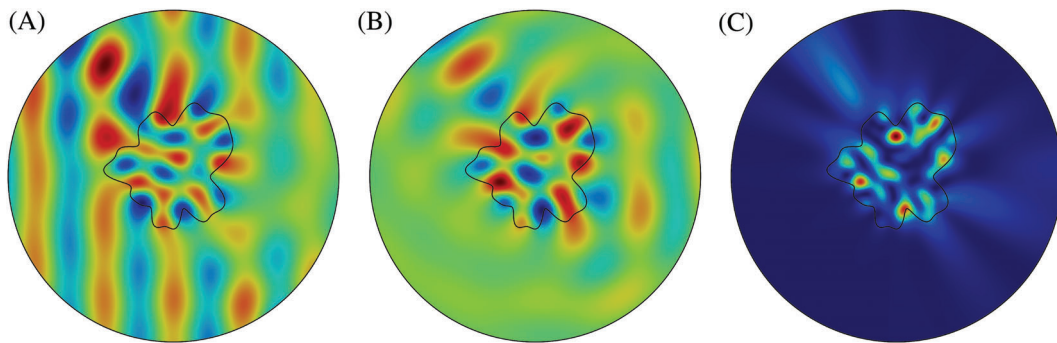


FIGURE 9 Scattering corresponding to the design Ω_s optimized for $\theta_c = 120^\circ$, $w = 15^\circ$, $n_s = 2$, $\omega = 5$, and $N = 15$. In panel (A) we show the corresponding visualization of $\text{Re } u$, in panel (B) $\text{Re } u^s$, and in panel (C) $|u^s|^2$, with u^s the solution of problem (4) and $u := u^s + e^{i\omega x_1}$ the total wave

computed with $N = 15$. Similarly as discussed above, the proposed shape optimization strategy reached very efficient designs. However, most optimal designs feature scattering tails at $\theta = 0^\circ$, and computations with fixed N indicate that this behavior worsens for higher frequencies specially for the cases $\theta_c \geq 90^\circ$. To provide better understanding on the resulting scattering patterns at $\theta = 0^\circ$, Figure 9 features plots corresponding to the case $\theta_c = 120^\circ$, $\omega = 5$, $n_s = 2$. From the scattered wave (b), it is evident that the scattering tail corresponds to a shadowed region in the total field plot (a). That is, the scattered wave interferes destructively with the incoming wave. As a consequence, the total wave exhibits a shadow behind the scatterer. For higher frequencies, stronger tails (scattering) or larger shadowed regions (total) are expected. As discussed above, these designs may be improved by using a higher refractive index n_s . Alternatively, the number of Fourier terms N may be increased and the penalization γ decreased, at the expense of obtaining highly oscillatory designs.

Finally, it is apparent from Figures 6, 7, and 8, that computation with low-order FE + PML seems to overestimate the scattering pattern of the optimal design when we compare it to the scattering pattern computed with high-order FE + DtN.

6 | DISCUSSION

The presented framework for the optimization for the strong directional scattering of dielectric nanorods can be extended in several interesting directions. For example, optimization of multiple rods may result in improved control of the scattering waves compared with what has been achieved here for a single rod. Hence, a possible extension aiming at the optimization of multiple numbers of rods using the representation (6) can be implemented in several ways. One option that can be straightforwardly implemented is to define a predefined set of rods (dimer, finite crystal), use a Fourier

representation for each cylinder, and run a numerical optimization scheme similarly as employed in this study. The number of design variables scales linearly with the number of rods. Additionally, one could consider special symmetries and use a mirror boundary condition on some of the rods for a dimer configuration. In this way, the cylinders can be represented with the same Fourier coefficients for both shape representations.

Another possibility is to assume an infinite periodic structure consisting of similar rods, as used in this work, where every rod in the structure has the same shape. To facilitate the computational load, it is feasible to impose periodic boundary conditions, and use a Bloch ansatz to represent the scattering problem. Then, the problem is set up in a unit cell, and the same numerical optimization scheme can be employed to find the optimal design as it has been presented in this work. However, we mention that the scattering efficiency evaluation and the adjoint equation must be modified slightly to fit this formulation.

The proposed optimization strategy can be implemented for acoustic waves or electromagnetic problems in 3D. An analogous shape representation to formula (6) can be set by employing spherical harmonics. For exterior conditions a PML or a DtN outgoing condition can be used. In the electromagnetic case, the full Maxwell's equations must be considered and the DtN is based on the Silver–Müller conditions. The extension of the shape formula and the transfinite interpolation in the three-dimensional setting is rather straightforward. The main computational challenges in this direction are the memory load, efficiency, and performance of the solver.

In general, local methods may be sensitive to the initial guess, but they show quick local convergence. On the other hand, global optimization algorithms typically require many function evaluations to improve on a candidate solution, whose corresponding objective function value is close to the globally optimal. Thus, one interesting alternative would be to combine the proposed method with a global optimization method, such as Bayesian optimization. The task for the global optimization method is then to produce good initial guesses for the proposed method. In such a case, the global method does not need to run to full convergence, and we can get the best of both worlds. For all our experiments, fortunately, the optimized design found using $\alpha_j = 0$, $\forall j$ as initial guess shows very good performance. For this problem, there was no need to use the above-mentioned strategy.

It would be interesting to compare the scattering efficiency of the proposed framework for different wave polarizations and cylinders made of all-dielectric, plasmonic, or mixed materials. Moreover, the current framework can be employed to design efficient polarization splitters and frequency band filters. Additionally, by performing minor modifications, we can use the developed framework for the design of efficient plasmonic nanoparticles with the application of cancer treatment in mind. Finally, the current framework can also be modified to be used for inverse problems in electromagnetics, in the specific case where the shape bounds of a solid object and its material properties are prescribed.

7 | CONCLUSIONS

We have proposed an effective strategy for the shape optimization of scatterers applied to Helmholtz problems. The resulting gradient based optimization strategy employs explicit differentiation of shapes with respect to the design variables by the use of transfinite interpolation and an exact adjoint method for the computation of sensitivities. Numerical computations indicate that for a wide range of target angles, frequencies, and refractive indexes we are able to obtain designs with outstanding scattering efficiencies. Overall, we have proposed a numerical strategy for obtaining optimal designs that exhibit remarkable directional scattering properties and can be used for applications involving light routing.

ACKNOWLEDGMENTS

The authors thank the anonymous reviewers for their valuable comments, and all the members of the Design Optimization Group at the Umit research lab for several enlightening discussions on numerical optimization for Helmholtz problems. This work was supported by the Kempe foundation under Grant No. SMK-1857 and the Swedish strategic research programme eSENCE.

DATA AVAILABILITY STATEMENT

The data that support the findings of this study are available from the corresponding author upon reasonable request.

ORCID

Juan C. Araújo  <https://orcid.org/0000-0002-0143-5554>

Eddie Wadbro  <https://orcid.org/0000-0001-8704-9584>

REFERENCES

- Wiecha PR, Cuche A, Arbouet A, et al. Strongly directional scattering from dielectric nanowires. *ACS Photonics*. 2017;4(8):2036-2046. <https://doi.org/10.1021/acsp Photonics.7b00423>.
- Zhang Q, Li M, Liao T, Cui X. Design of beam deflector, splitters, wave plates and metalens using photonic elements with dielectric metasurface. *Opt Commun*. 2018;411:93-100. <https://doi.org/10.1016/j.optcom.2017.11.011>.
- Zhuo X, Yip HK, Cui X, Wang J, Lin HQ. Colour routing with single silver nanorods. *Light Sci Appl*. 2019;8(1):39. <https://doi.org/10.1038/s41377-019-0150-1>.
- Shegai T, Chen S, Miljković VD, Zengin G, Johansson P, Käll M. A bimetallic nanoantenna for directional colour routing. *Nature Commun*. 2011;2(1):481. <https://doi.org/10.1038/ncomms1490>.
- Geffrin JM, García-Cámara B, Gómez-Medina R, et al. Magnetic and electric coherence in forward- and back-scattered electromagnetic waves by a single dielectric subwavelength sphere. *Nature Commun*. 2012;3(1):1171. <https://doi.org/10.1038/ncomms2167>.
- Li Y, Wan M, Wu W, Chen Z, Zhan P, Wang Z. Broadband zero-backward and near-zero-forward scattering by metallo-dielectric core-shell nanoparticles. *Sci Rep*. 2015;5(1):12491. <https://doi.org/10.1038/srep12491>.
- Luk'yanchuk BS, Voshchinnikov NV, Paniagua-Domínguez R, Kuznetsov AI. Optimum forward light scattering by spherical and spheroidal dielectric nanoparticles with high refractive index. *ACS Photonics*. 2015;2(7):993-999. <https://doi.org/10.1021/acsp Photonics.5b00261>.
- Länk NO, Johansson P, Käll M. Directional scattering and multipolar contributions to optical forces on silicon nanoparticles in focused laser beams. *Opt Express*. 2018;26(22):29074-29085. <https://doi.org/10.1364/OE.26.029074>.
- Alaee R, Filter R, Lehr D, Lederer F, Rockstuhl C. A generalized Kerker condition for highly directive nanoantennas. *Opt Lett*. 2015;40(11):2645-2648. <https://doi.org/10.1364/OL.40.002645>.
- Tanaka YY, Shimura T. Tridirectional polarization routing of light by a single triangular plasmonic nanoparticle. *Nano Lett*. 2017;17(5):3165-3170. <https://doi.org/10.1021/acs.nanolett.7b00672>.
- Person S, Jain M, Lapin Z, Sáenz JJ, Wicks G, Novotny L. Demonstration of zero optical backscattering from single nanoparticles. *Nano Lett*. 2013;13(4):1806-1809. <https://doi.org/10.1021/nl4005018>.
- Qin F, Zhang D, Liu Z, Zhang Q, Xiao J. Designing metal-dielectric nanoantenna for unidirectional scattering via Bayesian optimization. *Opt Express*. 2019;27(21):31075-31086. <https://doi.org/10.1364/OE.27.031075>.
- Barton JP, Alexander DR, Schaub SA. Internal and near-surface electromagnetic fields for a spherical particle irradiated by a focused laser beam. *J Appl Phys*. 1988;64(4):1632-1639. <https://doi.org/10.1063/1.341811>.
- Liu M, Xie Y, Feng T, Xu Y. Resonant broadband unidirectional light scattering based on genetic algorithm. *Opt Lett*. 2020;45(4):968-971. <https://doi.org/10.1364/OL.381431>.
- Jensen JS, Sigmund O. Topology optimization of photonic crystal structures: a high-bandwidth low-loss T-junction waveguide. *J Opt Soc Am B*. 2005;22(6):1191-1198. <https://doi.org/10.1364/JOSAB.22.001191>.
- Burger M. A framework for the construction of level set methods for shape optimization and reconstruction. *Interfaces Free Bound*. 2003;5:301-329.
- Molesky S, Lin Z, Piggott AY, Jin W, Vucković J, Rodriguez AW. Inverse design in nanophotonics. *Nat Photonics*. 2018;12(11):659-670. <https://doi.org/10.1038/s41566-018-0246-9>.
- Araújo JC, Engström C, Jarlebring E. Efficient resonance computations for Helmholtz problems based on a Dirichlet-to-Neumann map. *J Comput Appl Math*. 2018;330:177-192. <https://doi.org/10.1016/j.cam.2017.08.012>.
- Araújo JC, Campos C, Engström C, Roman JE. Computation of scattering resonances in absorptive and dispersive media with applications to metal-dielectric nano-structures. *J Comput Phys*. 2020;407:109220. <https://doi.org/10.1016/j.jcp.2019.109220>.
- Cessenat M. *Mathematical Methods in Electromagnetism*. Series on Advances in Mathematics for Applied Sciences. Vol 41. Singapore, Asia: World Scientific Publisher; 1996.
- Jackson JD. *Classical Electrodynamics*. 3rd ed. New York, NY: John Wiley & Sons; 1999.
- Rakić AD, Djurišić AB, Elazar JM, Majewski ML. Optical properties of metallic films for vertical-cavity optoelectronic devices. *Appl Opt*. 1998;37(22):5271-5283. <https://doi.org/10.1364/AO.37.005271>.
- Potthast R. Electromagnetic scattering from an orthotropic medium. *J Integral Equ Appl*. 1999;11(2):197-215. <https://doi.org/10.1216/jiea/1181074315>.
- Kirsch A, Lechleiter A. The operator equations of Lippmann-Schwinger type for acoustic and electromagnetic scattering problems in L_2 . *Appl Anal*. 2009;88(6):807-830. <https://doi.org/10.1080/00036810903042125>.
- Colton D, Kress R. *Inverse Acoustic and Electromagnetic Scattering Theory*. Studies in Advanced Mathematics. 3rd ed. New York, NY: Springer-Verlag; 2013.
- Ihlenburg F. *Finite Element Analysis of Acoustic Scattering*. Applied Mathematical Sciences. New York, NY: Springer; 1998.
- Melenk J, Sauter S. Convergence analysis for finite element discretizations of the Helmholtz equation with Dirichlet-to-Neumann boundary conditions. *Math Comput*. 2010;79:1871-1914. <https://doi.org/10.1090/S0025-5718-10-02362-8>.
- Schwab C. *p- and hp- Finite Element Methods: Theory and Applications in Solid and Fluid Mechanics*. Oxford, UK: Oxford University Press; 1998.
- Babuška I, Guo BQ. The H, P and HP version of the finite element method: basis theory and applications. *Adv Eng Softw*. 1992;15(3-4):159-174.
- Gordon WJ, Hall CA. Construction of curvilinear co-ordinate systems and applications to mesh generation. *Int J Numer Methods Eng*. 1973;7(4):461-477. <https://doi.org/10.1002/nme.1620070405>.

31. Gordon W, Hall C. Transfinite element methods: blending-function interpolation over arbitrary curved element domains. *Numer Math*. 1973;21(2):109-129. <https://doi.org/10.1007/BF01436298>.
32. Solin P, Segeth K, Dolezel I. *Higher-Order Finite Element Methods*. Studies in Advanced Mathematics. Boca Raton, FL; London, UK: Chapman & Hall/CRC Press; 2004.
33. Christensen P, Klarbring A. *An Introduction to Structural Optimization*. Solid Mechanics and Its Applications. Amsterdam, Netherlands: Springer; 2008.
34. Nocedal J, Wright SJ. *Numerical Optimization*. 2nd ed. New York, NY: Springer; 2006.
35. Thompson L, Pinsky PM. Complex wavenumber Fourier analysis of the p-version finite element method. *Comput Mech*. 1994;13(4):255-275. <https://doi.org/10.1007/BF00350228>.
36. Ainsworth M. Discrete dispersion relation for hp-version finite element approximation at high wave number. *SIAM J Numer Anal*. 2005;42(2):553-575.
37. Melenk JM, Sauter S. Wave-number explicit convergence analysis for Galerkin discretizations of the Helmholtz equation. *SIAM J Numer Anal*. 2011;49(3/4):1210-1243.
38. Alzetta G, Arndt D, Bangerth W, et al. The deal II library, version 9.0. *J Numer Math*. 2018;26(4):173-183. <https://doi.org/10.1515/jnma-2018-0054>.
39. Balay S, Gropp WD, McInnes LC, Smith BF. Efficient Management of Parallelism in Object Oriented Numerical Software Libraries. In: Arge E, Bruaset AM, Langtangen HP., eds. *Modern Software Tools in Scientific Computing*. Boston, MA: Birkhäuser Press; 1997: 163-202. https://doi.org/10.1007/978-1-4612-1986-6_8.
40. Schöberl J, Arnold A, Erb J, Melenk JM, Wihler TP. *C++11 Implementation of Finite Elements in NGSolve. Technical Report*. Vienna, Austria: Institute for Analysis and Scientific Computing, TU Wien; 2014.
41. Collino F, Monk P. The perfectly matched layer in curvilinear coordinates. *SIAM J Sci Comput*. 1998;19(6):2061-2090. <https://doi.org/10.1137/S1064827596301406>.

How to cite this article: Araújo JC, Wadbro E. Shape optimization for the strong directional scattering of dielectric nanorods. *Int J Numer Methods Eng*. 2021;122:3683-3704. <https://doi.org/10.1002/nme.6677>